International Journal of Hydrogen Energy 86 (2024) 24–35

Contents lists available at ScienceDirect

International Journal of Hydrogen Energy

journal homepage: www.elsevier.com/locate/he

Construction of In_2S_3–$In(OH)_3$–ZnS nanofibers for boosting photocatalytic hydrogen evolution

Yu-Cheng Chang [a,*], Shih-Yue Syu [a], Po-Chun Hsu [b]

[a] Department of Materials Science and Engineering, Feng Chia University, Taichung, 40724, Taiwan
[b] Pritzker School of Molecular Engineering, University of Chicago, Chicago, IL, 60637, USA

ARTICLE INFO

Keywords:
Hydrothermal
In_2S_3–$In(OH)_3$ nanosheets
Nanofibers
Photocatalytic hydrogen production
Heterostructures
Reusability

ABSTRACT

This research involved synthesizing In_2S_3–$In(OH)_3$ nanosheets through a simple hydrothermal method at a low reaction temperature. The impact of different indium chloride concentrations on the morphology and crystal structure of In_2S_3–$In(OH)_3$ nanostructures was investigated. The discussion extended to the photocatalytic hydrogen evolution of both In_2S_3–$In(OH)_3$ nanosheets and nanofibers. These findings indicated that In_2S_3–$In(OH)_3$ nanofibers exhibited optimal photocatalytic hydrogen production at various indium chloride concentrations. Furthermore, In_2S_3–$In(OH)_3$–ZnS heterostructures were created by reacting In_2S_3–$In(OH)_3$ nanosheets with varying concentrations of ZnS precursors. The study delved into the morphology and crystal structure, emphasizing photocatalytic hydrogen production in In_2S_3–$In(OH)_3$–ZnS nanofibers under different concentrations of ZnS precursors. Remarkably, the In_2S_3–$In(OH)_3$–ZnS nanofibers demonstrated exceptional hydrogen production efficiency, attributed to their larger specific surface area, improved blue light absorption, and reduced electron-hole pair recombination. Additionally, a comprehensive analysis explored the photocatalytic reaction mechanism, pH values, sacrificial reagents, sacrificial reagent concentrations, light source types, and intensities. These results highlighted the exceptional reusability of In_2S_3–$In(OH)_3$–ZnS nanofibers in photocatalytic hydrogen production, showcasing their potential for cost-effective and highly efficient applications in diverse fields.

1. Introduction

Recently, human-caused carbon dioxide emissions have caused global warming, leading to extreme climate anomalies, successive heavy rainfall, and drought [1,2]. Therefore, many researchers have always focused on effectively suppressing carbon dioxide emissions. Many countries have announced the goal of "2050 net zero". Net zero carbon emission is not only an urgent environmental protection issue but also a matter of international competitiveness [3]. Among the many energy sources, hydrogen energy has attracted the most attention. The main reason is that hydrogen only generates water after combustion or reaction through fuel cells and does not generate other wastes or carbon dioxide, an excellent alternative energy source [4]. In addition, hydrogen is also a suitable energy carrier [5]. Generally, the electricity generated by power plants cannot be stored in large quantities [6]. However, converting it into hydrogen can benefit long-term storage [7]. Although hydrogen energy exhibits excellent applications, most of its production methods can only be converted into hydrogen by converting fossil fuels into hydrogen after considering the cost-effectiveness, which causes carbon dioxide emissions [8]. Light energy is converted into hydrogen, which can further solve the energy problem and net zero carbon emissions [9,10].

At present, various excellent photocatalysts have been explored [11]. However, high-efficiency photocatalytic water splitting to generate hydrogen also needs to meet high stability and sufficient energy band edges to improve hydrogen evolution reaction (HER)/oxygen evolution reaction (OER) [12,13]. Researchers have adopted many Strategies to overcome these issues, including surface modification, nanostructure, and different material compositions to enhance photocatalytic performance [14–17]. One-dimensional (1D) nanomaterials, such as nanowires, nanofibers, and nanotubes, possess unique structures and dimensions that enhance charge transport and reduce electron-hole pair recombination more effectively than zero-dimensional nanomaterials [18,19]. The aforementioned benefits of one-dimensional nanomaterials can lead to a substantial enhancement in solar photocatalytic hydrogen production efficiency [20]. Compared with other methods, electrospinning technology is considered the most common method for commercially producing 1D nanofibers [21,22].

* Corresponding author.
E-mail address: yuchchang@fcu.edu.tw (Y.-C. Chang).

https://doi.org/10.1016/j.ijhydene.2024.08.403
Received 17 July 2024; Received in revised form 22 August 2024; Accepted 23 August 2024
Available online 28 August 2024

Electrospinning technology employs high-voltage static electricity to transform polymer solutions or melts into micro- or nanoscale fibers [23]. Electrospun fibers exhibit superior properties to those produced by traditional spinning methods, including a higher specific surface area, greater porosity, and enhanced thermal and electrical conductivity [24,25]. Electrospun nanofibers have extensive applications in tissue engineering, drug delivery, air and water filtration and separation, energy storage, and photocatalysis [23,25–28]. For achieving efficient photocatalytic water splitting to produce hydrogen, photocatalysts must satisfy several criteria, including broad solar light absorption, an appropriate band gap of less than 3.1 V, and a voltage exceeding 1.23 V, which is higher than that required for water electrolysis [29]. Metal oxides and metal sulfides are the most promising photocatalysts because they are easy to synthesize and have relatively stable energy band positions [13,30,31]. Titanium dioxide (TiO_2) is one of the most frequently converted into nanofibers using electrospinning technology among the various metal oxides [32]. However, the two main disadvantages of TiO_2 photocatalysts are the high recombination rate of photogenerated charge carriers and the ability only to absorb ultraviolet light, which severely limits their application in photocatalytic water splitting [33]. To overcome these two problems, TiO_2 composite nanofibers were often formed by combining TiO_2 nanofibers with different materials [33,34]. However, it is rare to directly combine different nanomaterials to form nanocomposites and then mix them with polymers to prepare composite nanofibers by electrospinning technology.

Zinc sulfide (ZnS) is a strong candidate for hydrogen production photocatalysis due to its ability to rapidly generate mobile photoexcited charge carriers, high conduction band potential for fast electron transfer, and active sites for hydrogen evolution without the need for metal co-catalysts [35,36]. However, its wide band gap (~3.6 eV) restricts its activity to UV light, and charge recombination remains a significant challenge [37,38]. To overcome these limitations, this study combines ZnS with indium compounds such as indium hydroxide ($In(OH)_3$) and indium sulfide (In_2S_3) to form In_2S_3–$In(OH)_3$–ZnS heterostructures. These heterostructures are fabricated into In_2S_3–$In(OH)_3$–ZnS nanofibers using electrospinning technology.

In the present work, we examined the impact of varying indium chloride concentrations on the morphology, crystal structure, optical properties, and photocatalytic water-splitting capabilities of In_2S_3–$In(OH)_3$ nanosheets. Furthermore, In_2S_3–$In(OH)_3$–ZnS nanocomposites were synthesized by incorporating In_2S_3–$In(OH)_3$ nanosheets with optimal hydrogen production performance into the reaction precursor of zinc sulfide. The characteristics of the resulting materials were thoroughly analyzed and discussed. Furthermore, electrospinning technology was used to create In_2S_3–$In(OH)_3$–ZnS nanofibers, followed by a thorough analysis and discussion to assess their efficiency in photocatalytic hydrogen production. The resulting In_2S_3–$In(OH)_3$–ZnS nanofibers exhibit a convenient, cost-effective, highly efficient photocatalytic performance and superior reusability. These attributes are expected to facilitate their application in various related fields.

2. Experimental

2.1. Chemicals

Indium(III) chloride hydrate ($InCl_3{\cdot}xH_2O$, 99.99%), thioacetamide (TAA, CH_3CSNH_2, 98%), sodium sulfide nonahydrate ($Na_2S{\cdot}9H_2O$, 98%), sodium sulfite (Na_2SO_3, 98%), and methanol (CH_3OH, 99%) were obtained from Alfa Aesar and used as received. Zinc nitrate hexahydrate ($Zn(NO_3)_2{\cdot}6H_2O$, 98%), poly(vinyl alcohol) (PVA, Mw: 89,000–98,000, 99%), and ethanol (C_2H_5OH, 99.8%) were obtained from Sigma-Aldrich and also used as received. All experimental procedures utilized deionized water with a resistance greater than 18 MΩ cm^{-1}.

2.2. Synthesis of In_2S_3–$In(OH)_3$ nanosheets

A facile hydrothermal process synthesized In_2S_3–$In(OH)_3$ nanosheets. Typically, a 20 mL aqueous solution with varying concentrations of $InCl_3{\cdot}xH_2O$ and 5 mM TAA was mixed and transferred into a 50 mL Teflon-lined autoclave. The reaction was carried out at 120 °C for 2 h. The resulting products were then washed several times with deionized water and collected via centrifugation. Finally, the products were dried at 70 °C for 2 h.

2.3. Synthesis of In_2S_3–$In(OH)_3$–ZnS heterostructures

A straightforward wet chemical method synthesized In_2S_3–$In(OH)_3$–ZnS heterostructures. In a standard procedure, different concentrations of the ZnS precursor (equimolar amounts of $Zn(NO_3)_2{\cdot}6H_2O$ and TAA) and 0.2 g of In_2S_3–$In(OH)_3$ nanosheets were dispersed in 50 mL of deionized water. This mixture was heated to 90 °C with vigorous stirring for 2 h. The resulting products were washed twice with deionized water and collected by centrifugation. Finally, the products were dried at 70 °C for 2 h.

2.4. Fabrication of In_2S_3–$In(OH)_3$–ZnS nanofibers

A straightforward electrospinning technique created In_2S_3–$In(OH)_3$–ZnS nanofibers. To prepare the electrospinning solution, 0.025 g of PVA and 0.0375 g of In_2S_3–$In(OH)_3$–ZnS heterostructures, with varying concentrations of ZnS precursors, were dissolved in 2.5 mL of deionized water under magnetic stirring for 2 h. The resulting precursor solution was then loaded into a syringe for electrospinning. An electrical potential of 13 kV was applied with a working distance of 13 cm. The solution was dispensed at a rate of 0.4 mL/h to produce nanofibers. The collected nanofibers were subsequently dried at 60 °C for 2 h.

2.5. Characterization

The synthesized samples' morphologies and microstructures were investigated using field-emission scanning electron microscopy (FE-SEM, Hitachi S-4800) and field-emission transmission electron microscopy (FE-TEM, JEOL-2100F). Crystal phases were determined by X-ray powder diffraction (XRD, Bruker D2 Phaser). Fourier transform infrared spectroscopy (FTIR, Bruker Vertex 80v) was used to analyze surface functional groups. X-ray photoelectron spectroscopy (XPS, ULVAC-PHI PHI 5000 Versaprobe II) evaluated the samples' surface elemental composition and chemical states. UV–vis diffuse reflectance spectra (DRS) were recorded with UV–vis spectroscopy (U-2900, Hitachi), and photoluminescence (PL) spectra were obtained using a LabRAM HR Evolution spectrophotometer (Horiba) with a 325 nm He–Cd laser. The specific surface areas were measured using the Brunauer-Emmett-Teller (BET) method with a high-resolution surface area and porosimetry analyzer (Micromeritics, ASAP 2020).

2.6. Photocatalytic hydrogen production tests

Photocatalytic hydrogen evolution experiments were carried out in a 50 mL sealed quartz bottle at room temperature and atmospheric pressure, utilizing a PCX-50B multichannel photochemical reaction system for 6 h. In a typical procedure, 0.0375 g of the synthesized nanopowders or nanofibers were added to a 50 mL aqueous solution containing the different concentrations of Na_2S (0–0.2 M) as a sacrificial agent. In addition, Na_2SO_4, CH_3OH, and C_2H_5OH at a concentration of 0.1 M were used as the other sacrificial agents. The different pH values of the aqueous solution with 0.1 M Na_2S solution were adjusted using 0.1 M HCl or 0.1 M NaOH, respectively. A 5W blue LED light (λ_{max} = 420 nm, 41.7 mW cm^{-2}) was the visible light source to promote water splitting into hydrogen [39]. The produced hydrogen gas was quantified using gas chromatography (GC, Shimadzu GC-2014) equipped with a thermal

conductivity detector (TCD) and a GC column (MS 5A 60/80).

3. Results and discussion

Fig. 1a shows the microstructure analysis of the In_2S_3–$In(OH)_3$ nanosheets, which were synthesized using a simple hydrothermal method with varying concentrations of $InCl_3$, as observed through FESEM. The $InCl_3$ concentrations are 2.5, 5, 7.5, and 10 mM, respectively. In_2S_3–$In(OH)_3$ nanosheet morphology tends to become bigger and bigger with the increase of $InCl_3$ concentrations. In addition, with the rise in the concentrations of $InCl_3$, the powder color gradually changed from orange to white-yellow. In general, the powder color of In_2S_3 and $In(OH)_3$ is orange and white, respectively [40]. Fig. 1b shows the crystal structure of the In_2S_3–$In(OH)_3$ nanosheets prepared under different $InCl_3$ concentrations by XRD. The XRD pattern of the In_2S_3–$In(OH)_3$ nanosheets (2.5 mM $InCl_3$) displays the distinctive peaks of In_2S_3 and $In(OH)_3$. For In_2S_3, the ten diffraction peaks at 27.4°, 29.5°, 33.2°, 43.7°, 53.8°, 60.2°, 61.3°, 66.6°, 70.6°, and 77.0° correspond to (109), (215), (0012), (318), (420), (431), (433), (523), (444), and (606) crystal planes of tetragonal In_2S_3, as identified by JCPDS card No. 73–1366. For $In(OH)_3$, the four diffraction peaks observed at 31.4°, 39.0°, 48.2°, and 51.5° match the (220), (222), (411), and (420) crystal planes of cubic $In(OH)_3$, as indicated by JCPDS card No. 85–1338. When indium chloride dissolves in water, it preferentially reacts with the hydroxide ions present, forming indium hydroxide. This reaction occurs more readily than indium sulfide formation involving indium and sulfide ions [41].

Fig. 2a presents the transmission electron microscope (TEM) image of the synthesized In_2S_3–$In(OH)_3$ nanosheets at the $InCl_3$ concentrations of 5 mM. It is evident that the In_2S_3–$In(OH)_3$ nanosheets aggregate, exhibiting morphology consistent with the observations from the FESEM image (Fig. 1a). Further examination with high-resolution TEM imaging uncovers lattice spacings of 0.269 nm corresponding to the (0012) plane of In_2S_3 and 0.399 nm corresponding to the (200) plane of $In(OH)_3$. These values align with JCPDS Card No. 73–1366 and JCPDS Card No. 85–1338, confirming the crystalline structures of In_2S_3 and $In(OH)_3$, as depicted in Fig. 2b. Selected area electron diffraction (SAED) analysis (Fig. 2c) verifies the polycrystalline nature of the product with crystal structures corresponding to both In_2S_3 and $In(OH)_3$. Energy-dispersive X-ray spectroscopy (EDS) provides insight into the compositional distribution of In_2S_3–$In(OH)_3$ nanosheet. Fig. 2d displays the EDS mapping images, which show the uniform distribution of In, S, and O elements within the nanosheets, confirming their structure as In_2S_3–$In(OH)_3$ nanosheets. The EDS spectrum (Fig. 2e) further confirms that the nanosheets consist only of In, S, O, and Cu (Cu attributed to the TEM grid), validating the compositional makeup of the synthesized In_2S_3–$In(OH)_3$ nanosheets.

To mitigate excessive aggregation of In_2S_3–$In(OH)_3$ nanosheets synthesized at different $InCl_3$ concentrations, this study employed electrospinning technology to blend them with PVA and create In_2S_3–$In(OH)_3$ nanofibers. The morphology is illustrated in Fig. 3a. As depicted, an increase in $InCl_3$ concentrations leads to more pronounced aggregation of the nanosheets in the resulting nanofibers. However, electrospinning prevents severe aggregation, as observed in the FESEM image (Fig. 1a). Additionally, Fourier-transform infrared spectroscopy (FTIR) was utilized to detect any chemical alterations in the functional groups of the PVA and In_2S_3–$In(OH)_3$ nanofibers, which were prepared through electrospinning at different $InCl_3$ concentrations, as illustrated in Fig. 3b. The characteristic peaks identified in PVA nanofibers consist of OH stretching (3300 cm^{-1}), CH_2 asymmetric stretching (2940 and 2910 cm^{-1}), symmetric bending of CH_2 (1426 cm^{-1}), (CH + OH) bending (1331 cm^{-1}), CH wagging (1239 cm^{-1}), C–O stretching (1090 cm^{-1}), CH_2 rocking (918 cm^{-1}), and CC stretching vibrations (850 cm^{-1}), respectively [42]. The FTIR spectra reveal that the growth of In_2S_3–$In(OH)_3$ nanofibers with different $InCl_3$ concentrations and the functional group positions match those of pure PVA nanofibers, indicating no chemical alterations. This result confirms that the materials synthesized undergo no chemical changes when combined with PVA nanofibers.

Photoluminescence (PL) spectroscopy analyzes fluorescence from the recombination of charge carriers, offering key insights into the behavior and separation of electron-hole pairs in semiconductor materials [43,44]. This study used a photoluminescence spectrometer with a 532 nm excitation wavelength to compare the electron and hole recombination rates of In_2S_3–$In(OH)_3$ nanosheets synthesized at various $InCl_3$ concentrations. The measurement range was 550–900 nm, as depicted in Fig. 4a. The excitation positions of In_2S_3 prepared at different $InCl_3$ concentrations were approximately 580–680 nm. This emission band is similar to literature findings, attributed to energy levels induced by indium, oxygen, and sulfur defects [45]. However, a slight deviation from literature values was observed, possibly due to the coexistence of In_2S_3 and $In(OH)_3$. The $In(OH)_3$ with oxygen defects can induce band formation of new energy levels, and variations may occur due to different preparation processes [46,47]. The In_2S_3–$In(OH)_3$ nanosheets synthesized at 5 mM $InCl_3$ concentrations exhibit significantly lower emission intensity than those prepared with other

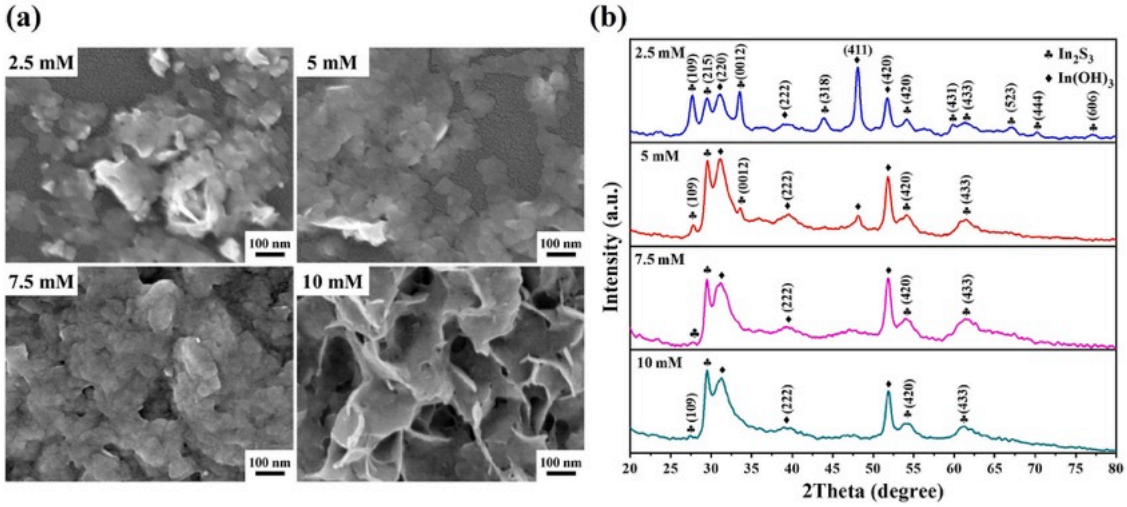

Fig. 1. The (a) FESEM images and (b) XRD patterns of In_2S_3–$In(OH)_3$ nanosheets grown at different $InCl_3$ concentrations. The $InCl_3$ concentrations of 2.5, 5, 7.5, and 10 mM, respectively.

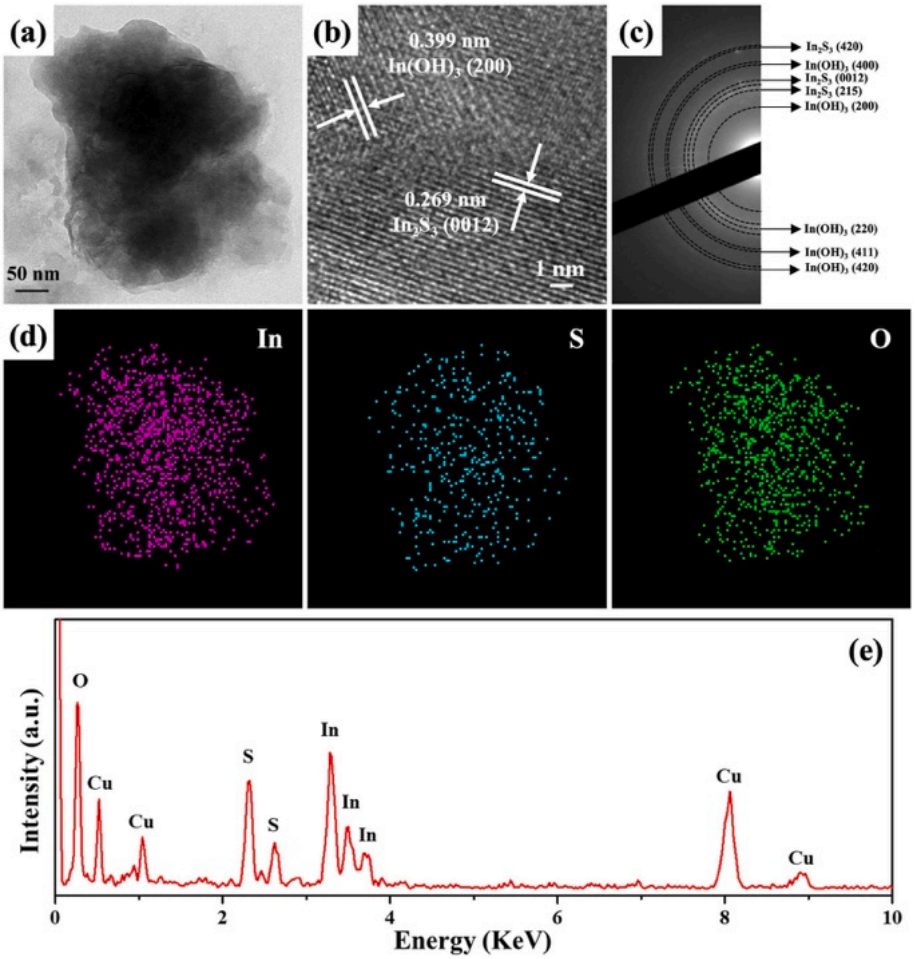

Fig. 2. The (a) FETEM image, (b) HRTEM image, (c) SAED pattern, (d) EDS mapping images, and (e) EDS pattern of In_2S_3–$In(OH)_3$ nanosheets.

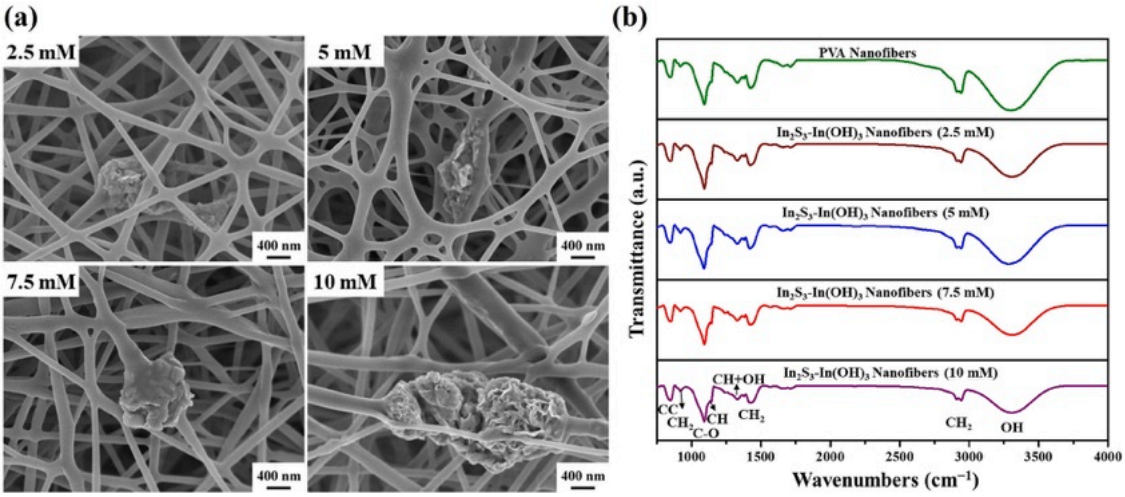

Fig. 3. The (a) FESEM images and (b) FTIR spectra of In_2S_3–$In(OH)_3$ nanofibers grown at different $InCl_3$ concentrations.

concentrations. This finding indicates that the material achieves the highest electron-hole separation rate at an $InCl_3$ concentration of 5 mM. It also confirms that varying $InCl_3$ concentrations can effectively decrease the electron-hole recombination rate.

In this study, In_2S_3–$In(OH)_3$ nanosheets were grown at different $InCl_3$ concentrations. The nanosheets were exposed to visible light from

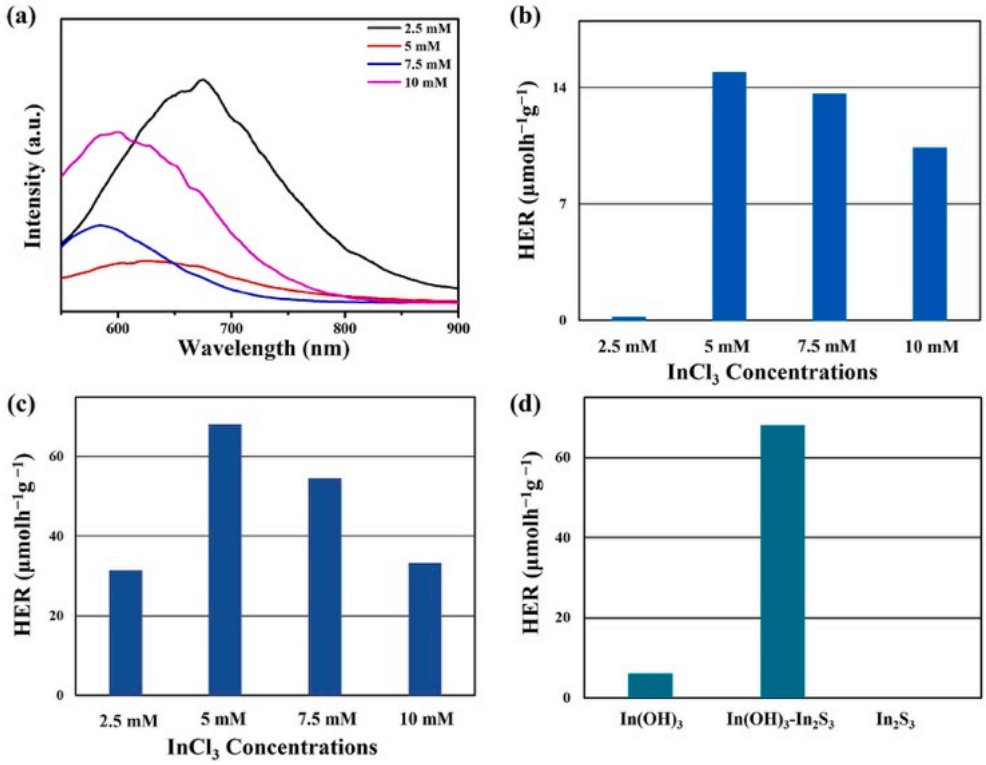

Fig. 4. (a) PL spectra, the average HER of (b) In_2S_3–$In(OH)_3$ nanosheets and (c) In_2S_3–$In(OH)_3$ nanofibers were grown at different $InCl_3$ concentrations. (d) The average HER of different nanofibers.

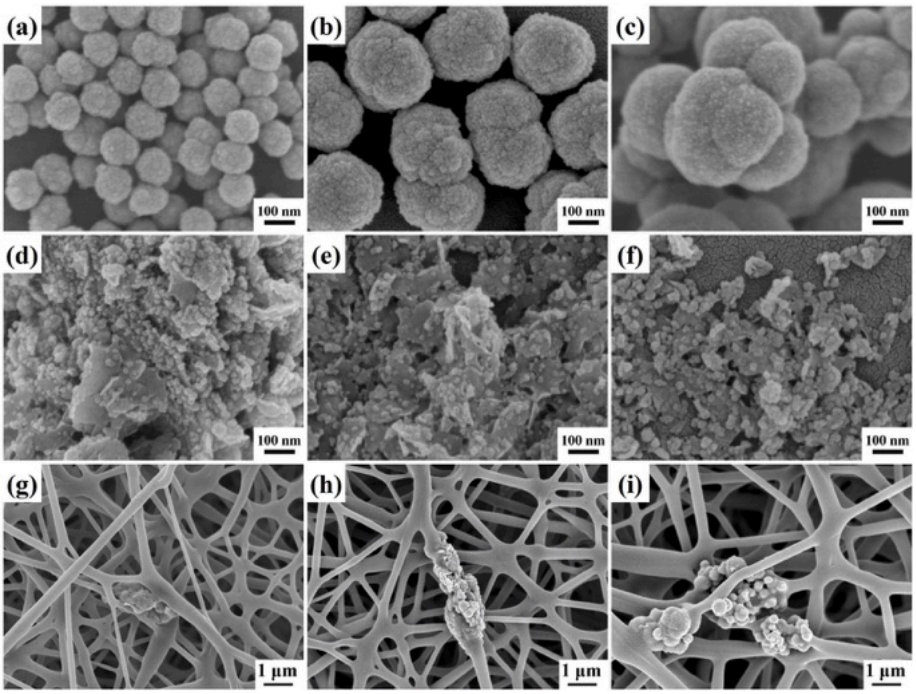

Fig. 5. The FESEM images of (a–c) ZnS nanospheres, (d–f) In_2S_3–$In(OH)_3$–ZnS heterostructures, and (g–i) In_2S_3–$In(OH)_3$ nanofibers grown at different ZnS precursor concentrations. The ZnS precursor concentrations of 5, 10, and 20 mM, respectively.

a 5W blue LED in a mixed aqueous solution containing 0.1 M Na_2S as a sacrificial agent with a pH of 12 for photocatalytic water splitting. The results are depicted in Fig. 4b. It is obtained that as-prepared In_2S_3–$In(OH)_3$ nanosheets exhibit the highest efficiency in photocatalytic hydrogen production at the $InCl_3$ concentrations of 5 mM. Furthermore, the photocatalytic water splitting efficiency at various $InCl_3$ concentrations is ranked in the following order: 5 mM, 7.5 mM, 10 mM, 2.5 mM. Interestingly, this trend contradicts the recombination rate intensity observed in previous PL measurements.

If the In_2S_3–$In(OH)_3$ nanosheets grown at different $InCl_3$ concentrations are further mixed with PVA and electrospun into nanofibers, as shown in Fig. 4c, the efficiency of photocatalytic hydrogen production retains a similar trend to that observed for the nanosheets. However, the photocatalytic efficiency is significantly enhanced, indicating that electrospinning can mitigate the aggregation issues seen in the nanosheets and improve the efficiency of photocatalytic hydrogen production. Additionally, Fig. 4d illustrates the efficiency of photocatalytic hydrogen production for nanofibers prepared through electrospinning from $In(OH)_3$ sub-microcubes, In_2S_3–$In(OH)_3$ nanosheets (5 mM $InCl_3$), and In_2S_3 nanosheets. It is observed that In_2S_3 nanofibers show negligible hydrogen production efficiency, while $In(OH)_3$ nanofibers exhibit relatively low hydrogen production efficiency. On the other hand, In_2S_3–$In(OH)_3$ nanofibers (5 mM $InCl_3$) demonstrate remarkably high photocatalytic hydrogen production efficiency. This improvement is credited to the heterojunction formed between In_2S_3 and $In(OH)_3$, which aids in separating photoexcited electrons and holes, thus enhancing the efficiency of photocatalytic hydrogen production.

To boost the efficiency of photocatalytic hydrogen production using In_2S_3–$In(OH)_3$ nanofibers, this research mixed the previously optimized In_2S_3–$In(OH)_3$ nanosheets with different concentrations of ZnS precursors. This formed In_2S_3–$In(OH)_3$–ZnS heterostructures through a wet chemical method. The FESEM images (Fig. 5a–c) reveal the ZnS nanospheres with comparable surface roughness were prepared under different concentrations of ZnS precursors (5 mM, 10 mM, and 20 mM) with sizes ranging from 50 to 80 nm, 120–250 nm, to 230–480 nm, respectively. The ZnS nanosphere sizes gradually increased with an increase in ZnS precursor concentrations. By incorporating the previously synthesized 0.2 g of In_2S_3–$In(OH)_3$ nanosheets (5 mM $InCl_3$) into different concentrations of ZnS precursors, followed by thorough mixing and wet chemical reaction for the formation of In_2S_3–$In(OH)_3$–ZnS heterostructures. The FESEM images (Fig. 5d–f) show the heterostructures obtained under different concentrations of ZnS precursors (5 mM, 10 mM, and 20 mM). With increased concentrations of ZnS precursors, the In_2S_3–$In(OH)_3$ nanosheets were gradually enveloped by ZnS nanospheres. Additionally, the sizes of ZnS nanospheres decreased compared to those without added In_2S_3–$In(OH)_3$ nanosheets, suggesting that the nanosheets may serve as a template to prevent ZnS self-aggregation. Furthermore, the FESEM images (Fig. 5g–i) display the In_2S_3–$In(OH)_3$–ZnS nanostructures prepared under different concentrations of ZnS precursors (5 mM, 10 mM, and 20 mM), which were subsequently electrospun into nanofibers using PVA. It is evident from the images that the In_2S_3–$In(OH)_3$–ZnS heterostructures have been encapsulated by PVA and forming nanofibers. The degree of aggregation appears to be reduced compared to the previous In_2S_3–$In(OH)_3$–ZnS heterostructures, confirming the effectiveness of the electrospinning process.

Fig. 6a illustrates the ZnS nanosphere produced via a wet chemical process with a ZnS precursor concentration of 10 mM. The morphology closely resembles that shown in the FESEM image (Fig. 5b). The HRTEM image of the ZnS nanosphere shows lattice spacings of 0.289 nm and

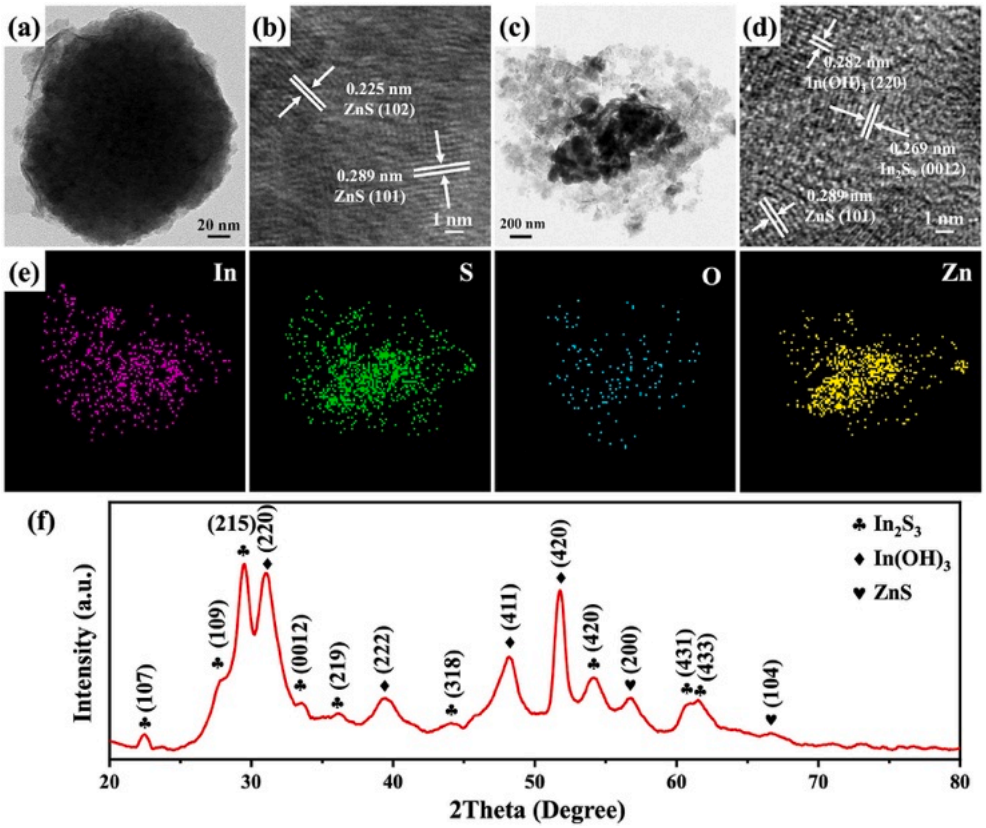

Fig. 6. The (a) FETEM image and (b) HRTEM image of ZnS nanospheres. (c) FETEM image, (d) HRTEM image, (e) EDS mapping images, and (f) XRD pattern of In_2S_3–$In(OH)_3$–ZnS heterostructures.

0.225 nm, which correspond to the (101) and (102) planes of ZnS, respectively. These measurements, as referenced by JCPDS Card No. 80-0007, can confirm the crystal structure of ZnS. Fig. 6c presents a FETEM image of the In_2S_3–$In(OH)_3$–ZnS nanostructure. The analysis shows that ZnS encapsulates the layered In_2S_3–$In(OH)_3$ structure. The HRTEM image (Fig. 6d) indicates lattice spacings of 0.289 nm for the (101) plane of ZnS, 0.282 nm for the (220) plane of $In(OH)_3$, and 0.269 nm for the (0012) plane of In_2S_3, corresponding to JCPDS Card No. 80-0007, JCPDS Card No. 85–1338, and JCPDS Card No. 73–1366, respectively. This result confirms the successful formation of In_2S_3–$In(OH)_3$–ZnS heterostructure. Fig. 6e reveals that In, S, O, and Zn elements with atomic concentrations of 16.31%, 40.87%, 17.46 %, and 25.36 %, respectively, are dispersed in the nanocomposite material, confirming the composition of the In_2S_3–$In(OH)_3$–ZnS heterostructure. Finally, Fig. 6f presents the XRD pattern of the In_2S_3–$In(OH)_3$–ZnS heterostructures, comparing them with JCPDS Card No. 80-0007, JCPDS Card No. 73–1366 and JCPDS Card No. 85–1338. In_2S_3, $In(OH)_3$, and ZnS are confirmed and consistent with the TEM results. XPS analysis (Fig. S1) confirmed that the In_2S_3–$In(OH)_3$–ZnS heterostructures are composed of In, O, S, and Zn, with specific binding energies indicating the presence of In^{3+} from $In(OH)_3$ or In_2S_3, S^{2-} from In_2S_3, and Zn^{2+} from ZnS [42,48,49].

In this study, In_2S_3–$In(OH)_3$–ZnS heterostructures were synthesized by incorporating a constant quantity of In_2S_3–$In(OH)_3$ nanosheets into varying concentrations of ZnS precursors through a wet chemical process. Subsequently, these structures were prepared into In_2S_3–$In(OH)_3$–ZnS nanofibers using electrospinning technology. The nanofibers were then subjected to visible light irradiation from a 5W blue LED light source in a mixed aqueous solution containing 0.1 M Na_2S as a sacrificial reagent for photocatalytic hydrogen evolution. Fig. 7a depicts the photocatalytic hydrogen evolution performance of In_2S_3–$In(OH)_3$ nanofibers, ZnS nanofibers, and In_2S_3–$In(OH)_3$–ZnS nanofibers grown with varying ZnS concentrations (5, 10, and 20 mM). The order of photocatalytic efficiency for hydrogen evolution is as follows: In_2S_3–$In(OH)_3$–ZnS nanofibers (10 mM), In_2S_3–$In(OH)_3$–ZnS nanofibers (5 mM), In_2S_3–$In(OH)_3$–ZnS nanofibers (20 mM), In_2S_3–$In(OH)_3$ nanofibers, and ZnS nanofibers (10 mM). Importantly, the In_2S_3–$In(OH)_3$–ZnS nanofibers (223.6 $\mu mol h^{-1} g^{-1}$) synthesized with a 10 mM ZnS precursor concentration demonstrate the highest photocatalytic hydrogen evolution efficiency. A comparative analysis of the photocatalytic hydrogen production activity of In_2S_3–$In(OH)_3$–ZnS nanofibers against other reported photocatalysts, as presented in Table S1, highlights their strong potential for practical applications.

To understand the reasons behind this phenomenon, the study examines the differences in specific surface area among the various materials, as depicted in Fig. 7b. The nitrogen adsorption-desorption isotherms for In_2S_3–$In(OH)_3$ nanosheets, ZnS nanospheres, and In_2S_3–$In(OH)_3$–ZnS heterostructures (from different ZnS precursor concentrations) display Type IV isotherms with hysteresis loops in the 0.45–0.95 P/P_0 range, indicating the presence of mesoporous structures. The mesopore sizes range from 2 to 50 nm. The specific surface area values, from highest to lowest, are 130.2 m^2/g (In_2S_3–$In(OH)_3$–ZnS heterostructures (10 mM)), 126.02 m^2/g (In_2S_3–$In(OH)_3$–ZnS heterostructures (5 mM)), 101.9 m^2/g (In_2S_3–$In(OH)_3$–ZnS heterostructures (20 mM)), 51.68 m^2/g (In_2S_3–$In(OH)_3$ nanosheets), and 13.45 m^2/g (ZnS nanospheres). This result indicates that the In_2S_3–$In(OH)_3$ nanosheets combined with ZnS provide a larger accessible specific surface area, increasing active sites and enhancing photocatalytic efficiency.

This study conducted an adsorption analysis using UV–vis diffuse reflectance spectra within the 350–800 nm range, as illustrated in Fig. 7c. The conspicuous augmentation in visible light adsorption is apparent in In_2S_3–$In(OH)_3$ nanosheets following composite reactions with varying concentrations of ZnS precursors. Furthermore, at the

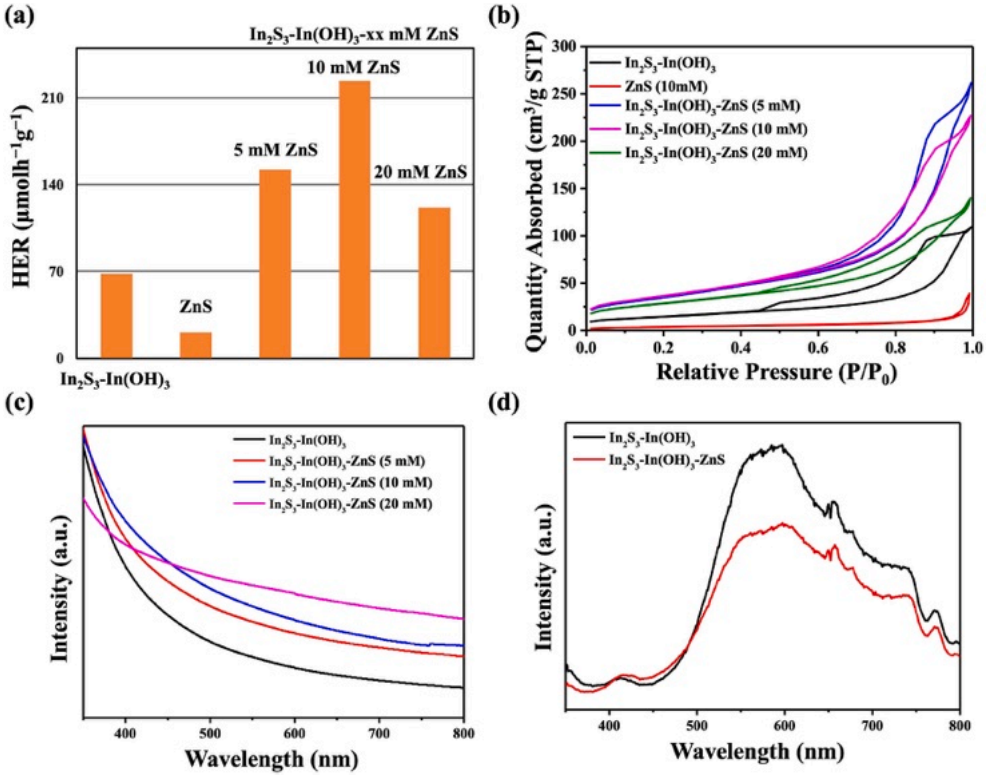

Fig. 7. (a) The average HER of In_2S_3–$In(OH)_3$, ZnS, and In_2S_3–$In(OH)_3$–ZnS nanofibers with different concentrations of ZnS precursors under blue LED light irradiation. (b) BET adsorption-desorption curve, (c) UV–vis diffuse reflectance spectra, and (d) PL spectra of In_2S_3–$In(OH)_3$ nanosheets and In_2S_3–$In(OH)_3$–ZnS heterostructures. (For interpretation of the references to color in this figure legend, the reader is referred to the Web version of this article.)

excitation wavelength of 420 nm, In_2S_3–$In(OH)_3$–ZnS heterostructures (10 mM) exhibit the highest absorption. This definitively confirms that In_2S_3–$In(OH)_3$–ZnS nanofibers synthesized under these conditions exhibit optimal hydrogen evolution efficiency. These findings highlight the significant potential of this composite material in utilizing light energy for improved performance in hydrogen evolution applications.

In this study, a PL spectrometer with a 325 nm wavelength excitation light source was used to compare the electron-hole pair recombination rates between In_2S_3–$In(OH)_3$ nanosheets and In_2S_3–$In(OH)_3$–ZnS heterostructures (10 mM). The detection range was 350–800 nm, as depicted in Fig. 7d. The emission intensity of the In_2S_3–$In(OH)_3$–ZnS heterostructures is notably lower than that of the In_2S_3–$In(OH)_3$ nanosheets. XPS analysis can confirm that the combination of In_2S_3–$In(OH)_3$ nanosheets and ZnS further caused an increase in oxygen defects, as shown in Fig. S2. Compared to In_2S_3–$In(OH)_3$ nanosheets, the S $2p_{3/2}$ and S $2p_{1/2}$ of sulfur vacancies of In_2S_3–$In(OH)_3$–ZnS heterostructures shift to the lower binding energy, demonstrating the additions of sulfur vacancies, as shown in Fig. S3. This phenomenon enhances the visible light absorption of $In(OH)_3$ and ZnS facilitates the separation of photogenerated electron-hole pairs and significantly boosts the efficiency of photocatalytic hydrogen production.

This mechanism through In_2S_3–$In(OH)_3$–ZnS nanofibers facilitates photocatalytic hydrogen production, as shown in Fig. 8. The material is coated onto indium tin oxide (ITO) glass using ion exchange resin, and cyclic voltammetry measurements are then conducted using a potentiostat [42]. The band positions of valence and conduction bands for In_2S_3, $In(OH)_3$, and ZnS are determined through a combination of absorbance values and impedance analysis, consistent with literature findings [50,51]. At a pH of 7, the energy band for hydrogen evolution is −0.43 eV, while oxygen evolution's is 0.83 eV [36]. Under blue LED light irradiation, In_2S_3 generates photogenerated electrons that transition from the valence band to the conduction band. Additionally, $In(OH)_3$ with oxygen defects and ZnS with sulfur defects can be activated by visible light, causing photogenerated electrons to transition from the valence band to the conduction band [52,53]. Subsequently, photogenerated electrons from the conduction band of $In(OH)_3$ migrate to the conduction band of ZnS and In_2S_3. Concurrently, photogenerated holes are transferred from $In(OH)_3$ to ZnS and In_2S_3. The PL analysis confirms the formation of heterostructures between In_2S_3–$In(OH)_3$ and ZnS, which can effectively separate photogenerated electrons and holes. The reduction half-reaction involves the reaction between hydrogen ions and electrons, producing hydrogen gas. On the other hand, the oxidation half-reaction is the reaction between water and holes, leading to the generation of oxygen, hydrogen ions, and electrons. The introduction of sacrificial reagents causes negative divalent sulfur ions to capture holes, forming irreversible disulfide ions. This process reduces the recombination rate of electrons and holes, ultimately enhancing the efficiency of photocatalytic hydrogen production [54,55]. This result proves that the heterostructure formed by In_2S_3–$In(OH)_3$ composite ZnS can have the best photocatalytic hydrogen production efficiency in the visible light band with the sacrificial reagent (Na_2S) benefit.

This study initially investigated the photocatalytic system of In_2S_3–$In(OH)_3$–ZnS nanofibers (10 mM) to demonstrate the potential impact of different pH values on hydrogen production efficiency. The results revealed that the optimum hydrogen production efficiency occurred at pH 12, as shown in Fig. 9a. Since pH values influence the charge properties on the surface of heterostructures and the extent of particle adsorption aggregation, they subsequently affect the effectiveness of photocatalytic hydrogen production [56]. The photocatalytic hydrogen production efficiency decreases sharply from pH 12 to pH 3. The possible reason is that hydrogen sulfide is generated when hydrochloric acid is added to adjust the pH. However, hydrogen sulfide reacts to form hydrosulfide ions (HS^-) and sulfur-negative divalent ions (S^{2-}), which only assist in photocatalytic hydrogen production in an alkaline environment. In contrast, hydrogen sulfide does not dissociate in neutral or acidic conditions [57,58]. Additionally, the impact of the isoelectric point cannot be overlooked. The isoelectric point of the photocatalyst primarily affects its adsorption-desorption performance. This study utilized a zeta potential analyzer to measure the isoelectric point and found that the isoelectric point for In_2S_3–$In(OH)_3$–ZnS nanofibers is approximately 6.4. According to the literature, the photocatalyst surface is negatively charged at the pH value of the isoelectric point, and above the isoelectric point, the surface becomes positively charged [59]. Therefore, when the surface is negatively charged, it easily attracts hydrogen ions, increasing the efficiency of photocatalytic hydrogen production [60,61]. Considering these factors, the photocatalytic hydrogen production efficiency of In_2S_3–$In(OH)_3$–ZnS nanofibers (10 mM) in Na_2S decreases from pH 12 to 3 across different pH values. Conversely, when the pH increases to pH 13, there is a decline in photocatalytic hydrogen production efficiency. This phenomenon may be due to the increased hydroxide ion concentration, which thermodynamically hinders the hydrogen production reaction [62]. The excess hydroxide ions may also combine with hydrogen ions, reducing them to water, thus decreasing the photocatalytic efficiency. Additionally, at

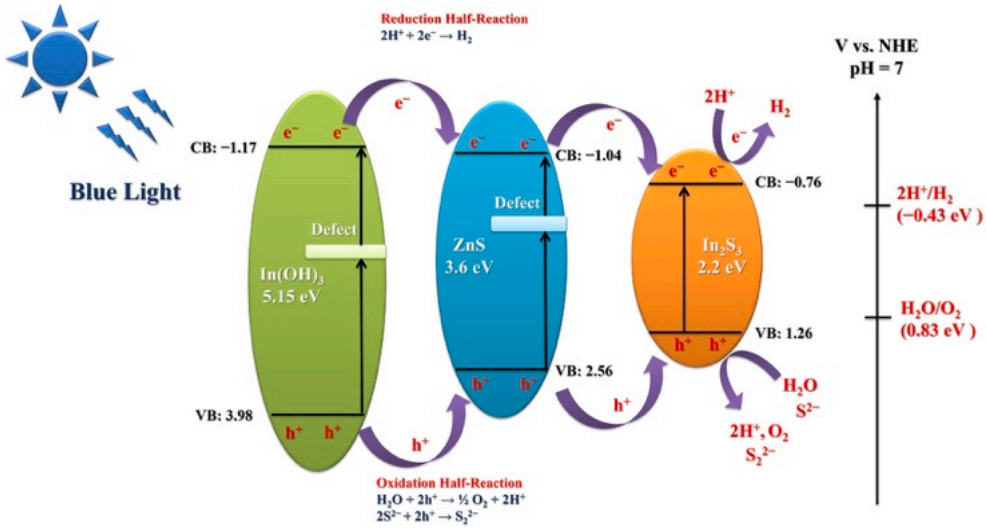

Fig. 8. The schematic diagram illustrates the photocatalytic mechanism of In_2S_3–$In(OH)_3$–ZnS nanofibers.

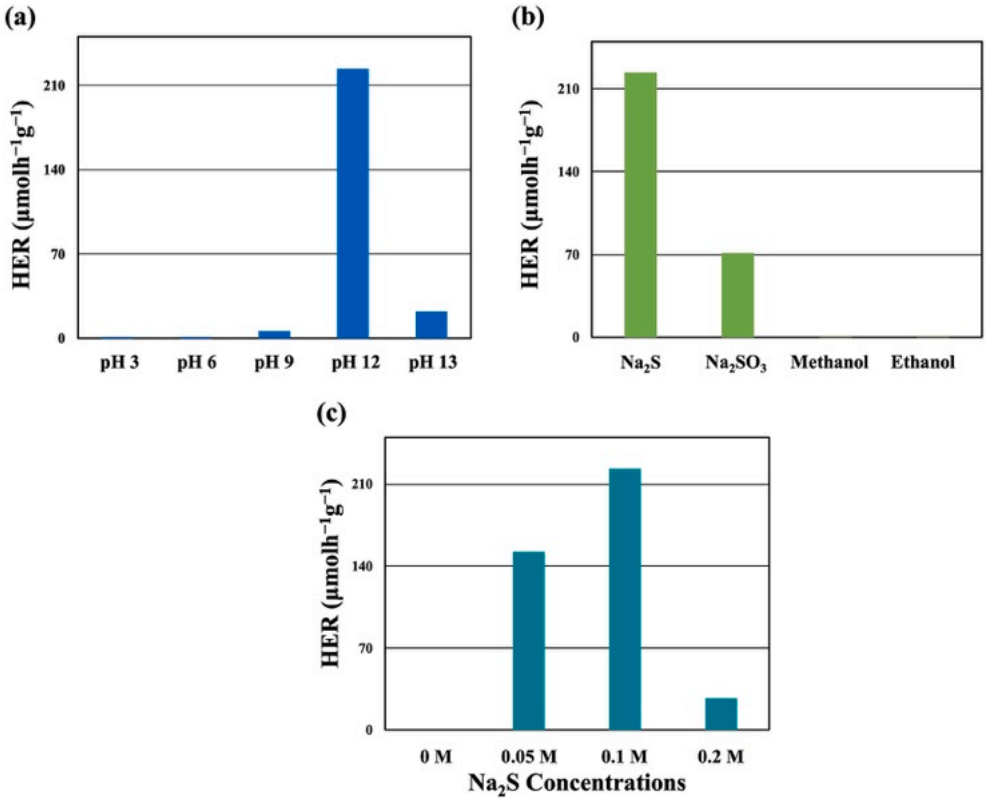

Fig. 9. The average HER of In_2S_3–$In(OH)_3$–ZnS nanofibers under (a) different pH values, (b) different sacrificial reagents, and (c) different concentrations of Na_2S.

higher pH values, sulfur-negative divalent ions may undergo hydrolysis, hindering their ability to assist in capturing electron holes and consequently reducing the efficiency of photocatalytic hydrogen production [60,63]. Therefore, this study further evaluated the hydrogen production efficiency using deionized water at pH 12 with various sacrificial agents.

Fig. 9b depicts the photocatalytic efficiency of In_2S_3–$In(OH)_3$–ZnS nanofibers (10 mM) under blue LED light irradiation, utilizing Na_2S, Na_2SO_4, CH_3OH, and C_2H_5OH as four different sacrificial agents at the concentrations of 0.1 M [64]. When Na_2S is used as a sacrificial agent, the photocatalytic efficiency is higher than that of CH_3OH, C_2H_5OH, and Na_2SO_4. The superior performance of Na_2S compared to Na_2SO_4 in photocatalytic hydrogen production is attributed to its enhanced hole-capturing ability, which effectively assists in the photocatalytic hydrogen production process. Na_2S is observed to improve the photocatalytic efficiency of metal sulfide materials compared to organic alcohols [55,64,65]. The underlying mechanism involves ions from inorganic sulfides adsorbing onto the material surface, reacting with holes, or recombining during material decomposition. This process reduces the corrosion rate of metal sulfide materials, minimizes sulfur defects, and enhances the stability of photocatalytic hydrogen production. Some literature also suggests inorganic sulfides are more readily oxidized than organic alcohols [66]. When Na_2S dissolves, it releases hydrogen sulfide ions (HS^-) and sulfide ions (S^{2-}). These ions can merge with photogenerated holes, thereby increasing the efficiency of photocatalytic hydrogen production [67,68]. These results demonstrate the influential role of Na_2S in improving the hydrogen production efficiency of In_2S_3–$In(OH)_3$–ZnS nanofibers.

Fig. 9c shows the photocatalytic efficiency of In_2S_3–$In(OH)_3$–ZnS nanofibers (10 mM) under blue LED light irradiation at various concentrations of Na_2S. The photocatalytic hydrogen production efficiency is zero without Na_2S, emphasizing the crucial role of sacrificial agents in photocatalytic hydrogen production. As the concentration of Na_2S increases, the photocatalytic efficiency also increases. However, after reaching a concentration of 0.2 M, the efficiency decreases. This may be attributed to sulfide anions being adsorbed on the catalyst surface, making it more challenging for electrons to reach the surface at high sulfide concentrations and decreasing photocatalytic efficiency. Other factors, such as the influence of van der Waals forces on ion density adsorbed at catalytic active sites, may also contribute to the reduction in photocatalytic efficiency. This study demonstrates that when the Na_2S concentration is 0.1 M, In_2S_3–$In(OH)_3$–ZnS nanofibers (10 mM) exhibit superior photocatalytic hydrogen production efficiency.

The study investigates the impact of different light sources on the photocatalytic hydrogen production efficiency of the as-prepared In_2S_3–$In(OH)_3$–ZnS nanofibers (10 mM). Fig. 10a and b depict the photocatalytic hydrogen production efficiency under blue and white LED light irradiation, comparing commercial photocatalysts (TiO_2 nanopowders and ZnO nanopowders) nanofibers, In_2S_3–$In(OH)_3$ nanofibers, and In_2S_3–$In(OH)_3$–ZnS nanofibers (10 mM). Notably, In_2S_3–$In(OH)_3$–ZnS nanofibers exhibit superior photocatalytic efficiency compared to In_2S_3–$In(OH)_3$ nanofibers, commercially available ZnO and TiO_2 nanofibers. This outcome demonstrates that forming heterostructures with sulfur defects enhances the photocatalytic effect, aligning with previous findings using different sacrificial reagents.

The manufactured In_2S_3–$In(OH)_3$–ZnS nanofibers outperform TiO_2 and ZnO nanofibers under similar photocatalytic conditions. This improvement is attributed to the fact that TiO_2 and ZnO are predominantly activated by UV light. In contrast, the light source falls within the visible light spectrum. Oxygen defects improve the material's ability to absorb visible light, thereby enhancing the efficiency of photocatalytic hydrogen production, although there are some limitations. Under white LED light, the photocatalytic efficiency of In_2S_3–$In(OH)_3$ nanofibers and In_2S_3–$In(OH)_3$–ZnS nanofibers is reduced compared to blue LED light.

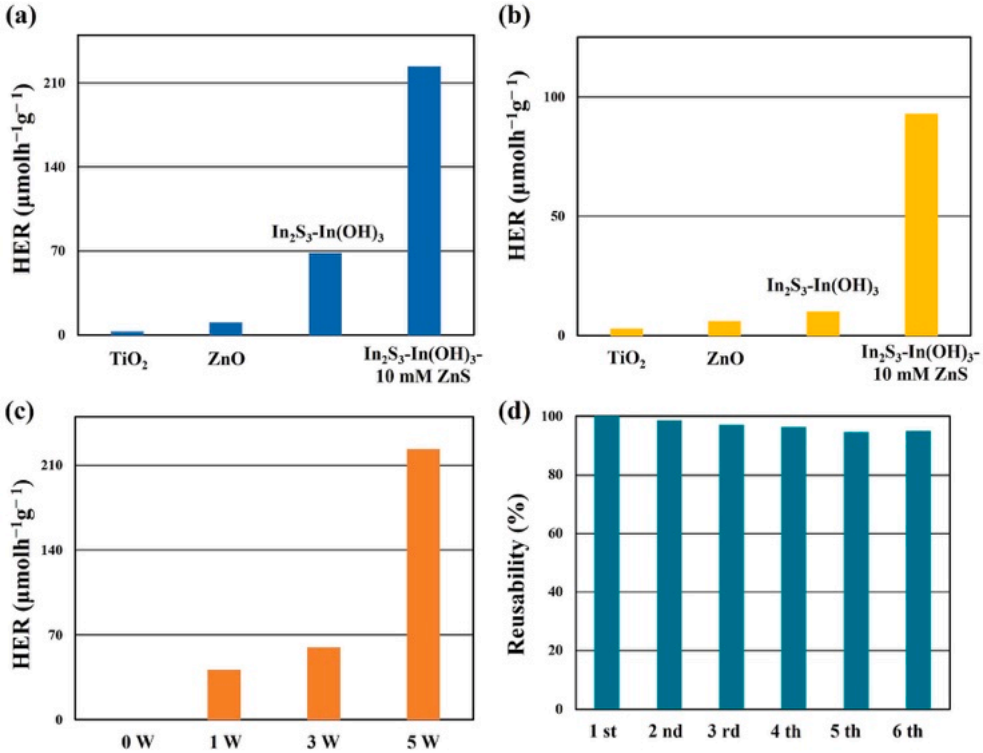

Fig. 10. The average HER of In_2S_3–$In(OH)_3$–ZnS nanofibers under (a) blue and (b) white LED light irradiation. (c) The average HER of In_2S_3–$In(OH)_3$–ZnS nanofibers under blue LED light irradiation with different power. (d) A reusability test of In_2S_3–$In(OH)_3$–ZnS nanofibers for photocatalytic hydrogen production under blue LED light irradiation. (For interpretation of the references to color in this figure legend, the reader is referred to the Web version of this article.)

This is likely due to the 5W power disperses energy across multiple wavelengths. In contrast, blue light increases photocatalytic efficiency with its concentrated energy in a single wavelength. This finding underscores the superior photocatalytic hydrogen production efficiency achievable with blue LED light compared to white LED light.

Furthermore, an investigation into the efficiency of hydrogen production through photocatalytic water decomposition by In_2S_3–$In(OH)_3$–ZnS nanofibers under different blue LED light intensities is presented in Fig. 10c. The findings show a steady improvement in efficiency with increasing wattage of the blue LED light source, implying that higher irradiance generates more electron-hole pairs, thereby boosting the efficiency of photocatalytic hydrogen production.

Fig. 10d presents the results of six consecutive cycles to assess the stability and reusability of In_2S_3–$In(OH)_3$–ZnS nanofibers in the photocatalytic hydrogen production process. Under optimal photocatalytic conditions, the In_2S_3–$In(OH)_3$–ZnS nanofibers maintain 95.1% of their hydrogen production performance after six cycles. In addition, the XRD patterns (Fig. S4) of the sample before and after six cycles revealed no new peaks, verifying that the crystal structure of the sample has remained intact. This outcome emphasizes the stability and reusability of In_2S_3–$In(OH)_3$–ZnS nanofibers in photocatalytic hydrogen production, showcasing their potential for various applications in future research.

4. Conclusions

This research used hydrothermal methods to synthesize In_2S_3–$In(OH)_3$ nanosheets. The effect of varying $InCl_3$ concentrations on the morphology and crystal structure of the resulting In_2S_3–$In(OH)_3$ nanosheets was examined. The influence of the nanosheets and nanofibers on photocatalytic hydrogen production was explored. The findings indicated that the photocatalyst achieves optimal hydrogen production efficiency by using the appropriate concentration of $InCl_3$ and converting the In_2S_3–$In(OH)_3$ nanosheets into nanofibers. To further enhance the photocatalytic performance of the In_2S_3–$In(OH)_3$ nanofibers, the study synthesized heterostructures by reacting the previously optimized In_2S_3–$In(OH)_3$ nanosheets with different concentrations of ZnS precursor. The effects on morphology and crystal structure were investigated, as well as the impact of photocatalytic hydrogen production. This research demonstrated that the In_2S_3–$In(OH)_3$–ZnS nanofibers (10 mM ZnS precursors) exhibited the best hydrogen production efficiency. These improvements were ascribed to its larger specific surface area, enhanced absorption in the blue light spectrum, and inhibition of electron-hole recombination, which collectively boost the efficiency of photocatalytic hydrogen generation. Furthermore, the study conducted in-depth analyses and discussions on the photocatalytic reaction mechanism, pH values, sacrificial reagents, sacrificial reagent concentrations, light sources, and light source intensities, aiming to identify the optimal conditions for photocatalytic hydrogen production. The In_2S_3–$In(OH)_3$–ZnS nanofibers also demonstrated excellent photocatalytic hydrogen production repeatability. These nanofibers offer a convenient, cost-effective, highly efficient, and reusable photocatalyst, which holds potential for applications in various fields.

CRediT authorship contribution statement

Yu-Cheng Chang: Writing – review & editing, Writing – original draft, Visualization, Supervision, Software, Resources, Project administration, Investigation, Data curation, Conceptualization. **Shih-Yue Syu:** Methodology, Formal analysis, Data curation. **Po-Chun Hsu:** Resources, Methodology, Conceptualization.

Declaration of competing interest

The authors declare the following financial interests/personal relationships which may be considered as potential competing interests: Yu-Cheng Chang reports financial support was provided by National Science and Technology Council. If there are other authors, they declare that they have no known competing financial interests or personal relationships that could have appeared to influence the work reported in this paper.

Acknowledgments

The authors sincerely appreciate the financial support from the National Science and Technology Council, Taiwan, under Grant Nos. NSTC 112-2221-E-035-017-MY3 and NSTC 113-2221-E-035-023-MY3.

Appendix ASupplementary data

Supplementary data to this article can be found online at https://doi.org/10.1016/j.ijhydene.2024.08.403.

References

[1] Anderson TR, Hawkins E, Jones PD. CO2, the greenhouse effect and global warming: from the pioneering work of Arrhenius and Callendar to today's Earth System Models. Endeavour 2016;40:178–87.
[2] Zuberi MJS, Ali SF. Greenhouse effect reduction by recovering energy from waste landfills in Pakistan. Renew Sustain Energy Rev 2015;44:117–31.
[3] Garvey A, Norman JB, Barrett J. Technology and material efficiency scenarios for net zero emissions in the UK steel sector. J Clean Prod 2022;333:130216.
[4] Amin M, Shah HH, Fareed AG, Khan WU, Chung E, Zia A, et al. Hydrogen production through renewable and non-renewable energy processes and their impact on climate change. Int J Hydrogen Energy 2022;47:33112–34.
[5] Oshiro K, Fujimori S. Role of hydrogen-based energy carriers as an alternative option to reduce residual emissions associated with mid-century decarbonization goals. Appl Energy 2022;313:118803.
[6] Hadjipaschalis I, Poullikkas A, Efthimiou V. Overview of current and future energy storage technologies for electric power applications. Renew Sustain Energy Rev 2009;13:1513–22.
[7] Rasul MG, Hazrat MA, Sattar MA, Jahirul MI, Shearer MJ. The future of hydrogen: Challenges on production, storage and applications. Energy Convers Manag 2022; 272:116326.
[8] Tashie-Lewis BC, Nnabuife SG. Hydrogen production, distribution, storage and power conversion in a hydrogen Economy - a technology review. Chem Eng J Advan 2021;8:100172.
[9] Dutta S. A review on production, storage of hydrogen and its utilization as an energy resource. J Ind Eng Chem 2014;20:1148–56.
[10] Parthasarathy P, Narayanan KS. Hydrogen production from steam gasification of biomass: influence of process parameters on hydrogen yield – a review. Renew Energy 2014;66:570–9.
[11] Li H, Zhou Y, Tu W, Ye J, Zou Z. State-of-the-Art Progress in diverse heterostructured photocatalysts toward promoting photocatalytic performance. Adv Funct Mater 2015;25:998–1013.
[12] Chang Y-C, Tasi C-L, Ko F-H. Construction of ZnIn2S4/ZnO heterostructures with enhanced photocatalytic decomposition and hydrogen evolution under blue LED irradiation. Int J Hydrogen Energy 2021;46:10281–92.
[13] Kment S, Riboni F, Pausova S, Wang L, Wang L, Han H, et al. Photoanodes based on TiO2 and α-Fe2O3 for solar water splitting – superior role of 1D nanoarchitectures and of combined heterostructures. Chem Soc Rev 2017;46:3716–69.
[14] Hainer AS, Hodgins JS, Sandre V, Vallieres M, Lanterna AE, Scaiano JC. Photocatalytic hydrogen generation using metal-decorated TiO2: sacrificial Donors vs True water splitting. ACS Energy Lett 2018;3:542–5.
[15] Kudo A, Miseki Y. Heterogeneous photocatalyst materials for water splitting. Chem Soc Rev 2009;38:253–78.
[16] Wu M, Yan J-M, Zhang X-W, Zhao M, Jiang Q. Ag2O modified g-C3N4 for highly efficient photocatalytic hydrogen generation under visible light irradiation. J Mater Chem A 2015;3:15710–4.
[17] Guo B, Zhao J, Xu Y, Wen X, Ren X, Huang X, et al. Noble metal Phosphides supported on CoNi metaphosphate for efficient Overall water splitting. ACS Appl Mater Interfaces 2024;16:8939–48.
[18] Lang X, Gopalan S, Fu W, Ramakrishna S. Photocatalytic water splitting utilizing electrospun semiconductors for solar hydrogen generation: fabrication, modification and performance. Bull Chem Soc Jpn 2020;94:8–20.
[19] Chen H, Yang S. Hierarchical nanostructures of metal oxides for enhancing charge separation and transport in photoelectrochemical solar energy conversion systems. Nanoscale Horizons 2016;1:96–108.
[20] Khan K, Tao X, Zhao Y, Zeng B, Shi M, Ta N, et al. Spatial separation of dual-cocatalysts on one-dimensional semiconductors for photocatalytic hydrogen production. J Mater Chem A 2019;7:15607–14.
[21] Verma S, Sinha-Ray S, Sinha-Ray S. Electrospun CNF supported Ceramics as electrochemical catalysts for water splitting and fuel cell: a review. Polymers 2020; 12.
[22] Shi X-L, Cao J, Li X, Zhang J, Gong H, Liu S. Polyetheretherketone fiber-supported polyethylene glycols for phase-transfer catalysis in its surface layer. Colloids Surf A Physicochem Eng Asp 2024;694:134160.
[23] Chronakis IS. Novel nanocomposites and nanoceramics based on polymer nanofibers using electrospinning process—a review. J Mater Process Technol 2005; 167:283–93.
[24] Teo WE, Ramakrishna S. A review on electrospinning design and nanofibre assemblies. Nanotechnology 2006;17:R89.
[25] Ahmed FE, Lalia BS, Hashaikeh R. A review on electrospinning for membrane fabrication: Challenges and applications. Desalination 2015;356:15–30.
[26] Huang Z-M, Zhang YZ, Kotaki M, Ramakrishna S. A review on polymer nanofibers by electrospinning and their applications in nanocomposites. Compos Sci Technol 2003;63:2223–53.
[27] Bai S, Guo W, Sun J, Li J, Tian Y, Chen A, et al. Synthesis of SnO2–CuO heterojunction using electrospinning and application in detecting of CO. Sensor Actuator B Chem 2016;226:96–103.
[28] Hu X, Liu S, Zhou G, Huang Y, Xie Z, Jing X. Electrospinning of polymeric nanofibers for drug delivery applications. J Contr Release 2014;185:12–21.
[29] Bard AJ, Fox MA. Artificial photosynthesis: solar splitting of water to hydrogen and oxygen. Acc Chem Res 1995;28:141–5.
[30] Moniz SJA, Shevlin SA, Martin DJ, Guo Z-X, Tang J. Visible-light driven heterojunction photocatalysts for water splitting – a critical review. Energy Environ Sci 2015;8:731–59.
[31] Ran J, Zhang J, Yu J, Jaroniec M, Qiao SZ. Earth-abundant cocatalysts for semiconductor-based photocatalytic water splitting. Chem Soc Rev 2014;43: 7787–812.
[32] Song J, Guan R, Xie M, Dong P, Yang X, Zhang J. Advances in electrospun TiO2 nanofibers: design, construction, and applications. Chem Eng J 2022;431:134343.
[33] Chang Y-C, Zeng C-J, Chen C-Y, Tsay C-Y, Lee G-J, Wu JJ. NiS/Pt loaded on electrospun TiO2 nanofiber with enhanced visible-light-driven photocatalytic hydrogen production. Mater Res Bull 2023;157:112041.
[34] Etacheri V, Di Valentin C, Schneider J, Bahnemann D, Pillai SC. Visible-light activation of TiO2 photocatalysts: Advances in theory and experiments. J Photochem Photobiol, C 2015;25:1–29.
[35] Kurnia F, Ng YH, Amal R, Valanoor N, Hart JN. Defect engineering of ZnS thin films for photoelectrochemical water-splitting under visible light. Sol Energy Mater Sol Cells 2016;153:179–85.
[36] Lee G-J, Anandan S, Masten SJ, Wu JJ. Photocatalytic hydrogen evolution from water splitting using Cu doped ZnS microspheres under visible light irradiation. Renew Energy 2016;89:18–26.
[37] Lee G-J, Wu JJ. Recent developments in ZnS photocatalysts from synthesis to photocatalytic applications — a review. Powder Technol 2017;318:8–22.
[38] Bak D, Kim JH. Oxidation driven ZnS Core-ZnO shell photocatalysts under controlled oxygen atmosphere for improved photocatalytic solar water splitting. J Power Sources 2018;389:70–6.
[39] Zhao H, Chordiya K, Leukkunen P, Popov A, Upadhyay Kahaly M, Kordas K, et al. Dimethylammonium iodide stabilized bismuth halide perovskite photocatalyst for hydrogen evolution. Nano Res 2021;14:1116–25.
[40] Li Y, Li T, Tian J, Wang X, Cui H. TiO2 nanobelts decorated with In2S3 nanoparticles as photocatalysts with enhanced full-solar-spectrum (UV–vis–NIR) photocatalytic activity toward the degradation of tetracycline. Part Part Syst Char 2017;34:1700127.
[41] Li H, Yuan Z, Bittencourt C, Li X, Li W, Chen M, et al. Anion exchange synthesis of hollow β-In2S3 nanoparticles: adsorption and visible light photocatalytic performances. J Environ Chem Eng 2019;7:102910.
[42] Chang Y-C, Syu S-Y, Lu M-Y. Fabrication of In(OH)3–In2S3–Cu2O nanofiber for highly efficient photocatalytic hydrogen evolution under blue light LED excitation. Int J Hydrogen Energy 2023;48:9318–32.
[43] Chang Y-C, Bi J-N, Pan K-Y, Chiao Y-C. Microwave-assisted synthesis of SnO2@ ZnIn2S4 composites for highly efficient photocatalytic hydrogen evolution. Materials2024.
[44] Lin Y-R, Chang Y-C, Ko F-H. One-pot microwave-assisted synthesis of In2S3/In2O3 nanosheets as highly active visible light photocatalysts for seawater splitting. Int J Hydrogen Energy 2024;52:953–63.
[45] Jayakrishnan R, John TT, Kartha CS, Vijayakumar K, Abe T, Kashiwaba Y. Defect analysis of sprayed β-In2S3 thin films using photoluminescence studies. Semicond Sci Technol 2005;20:1162.
[46] Motta F, Lima R, Marques A, Li M, Leite E, Varela JA, et al. Indium hydroxide nanocubes and microcubes obtained by microwave-assisted hydrothermal method. J Alloys Compd 2010;497:L25–8.
[47] Tavares M, Lovisa L, Araújo V, Longo E, Li M, Nascimento RM, et al. Fast photocatalytic degradation of an organic dye and photoluminescent properties of Zn doped in (OH) 3 obtained by the microwave-assisted hydrothermal method. Mater Sci Semicond Process 2014;27:1036–41.
[48] He Z, Wang Y, Dong X, Zheng N, Ma H, Zhang X. Indium sulfide nanotubes with sulfur vacancies as an efficient photocatalyst for nitrogen fixation. RSC Adv 2019; 9:21646–52.
[49] Chang Y-C, Chiao Y-C, Fun Y-X. Cu2O/CuS/ZnS nanocomposite boosts blue LED-light-driven photocatalytic hydrogen evolution. Catalysts2022.
[50] Gu Y, Xu Z, Guo L, Wan Y. ZnO nanoplate-induced phase transformation synthesis of the composite ZnS/In (OH) 3/In 2 S 3 with enhanced visible-light photodegradation activity of pollutants. CrystEngComm 2014;16:10997–1006.

[51] Huang J-Y, Hsieh P-L, Naresh G, Tsai H-Y, Huang MH. Photocatalytic activity suppression of CdS nanoparticle-decorated Cu2O Octahedra and rhombic Dodecahedra. J Phys Chem C 2018;122:12944–50.
[52] Jean S-T, Her Y-C. Growth mechanism and cathodoluminescence properties of indium hydroxide nanocubes synthesized from a simple aqueous solution. CrystEngComm 2011;13:2324–30.
[53] Zhu Y-C, Bando Y, Xue D-F. Spontaneous growth and luminescence of zinc sulfide nanobelts. Appl Phys Lett 2003;82:1769–71.
[54] Li Y, He F, Peng S, Lu G, Li S. Photocatalytic H2 evolution from NaCl saltwater over ZnS1− x− 0.5 yOx (OH) y–ZnO under visible light irradiation. Int J Hydrogen Energy 2011;36:10565–73.
[55] Bao N, Shen L, Takata T, Domen K. Self-templated synthesis of nanoporous CdS nanostructures for highly efficient photocatalytic hydrogen production under visible light. Chem Mater 2008;20:110–7.
[56] Puga AV. Photocatalytic production of hydrogen from biomass-derived feedstocks. Coord Chem Rev 2016;315:1–66.
[57] Jang JS, Li W, Oh SH, Lee JS. Fabrication of CdS/TiO2 nano-bulk composite photocatalysts for hydrogen production from aqueous H2S solution under visible light. Chem Phys Lett 2006;425:278–82.
[58] Teets TS, Nocera DG. Photocatalytic hydrogen production. Chem Commun 2011; 47:9268–74.
[59] Ghasemi Z, Younesi H, Zinatizadeh AA. Kinetics and thermodynamics of photocatalytic degradation of organic pollutants in petroleum refinery wastewater over nano-TiO2 supported on Fe-ZSM-5. J Taiwan Inst Chem Eng 2016;65:357–66.
[60] Rao VN, Reddy NL, Kumari MM, Ravi P, Sathish M, Neppolian B, et al. Synthesis of titania wrapped cadmium sulfide nanorods for photocatalytic hydrogen generation. Mater Res Bull 2018;103:122–32.
[61] Lin W-C, Yang W-D, Huang I-L, Wu T-S, Chung Z-J. Hydrogen production from methanol/water photocatalytic decomposition using Pt/TiO2− x N x catalyst. Energy Fuel 2009;23:2192–6.
[62] Enzweiler H, Yassue-Cordeiro PH, Schwaab M, Barbosa-Coutinho E, Olsen Scaliante MHN, Fernandes NRC. Catalyst concentration, ethanol content and initial pH effects on hydrogen production by photocatalytic water splitting. J Photochem Photobiol, A: Chem 2020;388:112051.
[63] Sadovnikov S, Kozlova E, Gerasimov EY, Rempel A. Photocatalytic hydrogen evolution from aqueous solutions on nanostructured Ag2S and Ag2S/Ag. Catal Commun 2017;100:178–82.
[64] Wang L, Wang W, Shang M, Yin W, Sun S, Zhang L. Enhanced photocatalytic hydrogen evolution under visible light over Cd1− xZnxS solid solution with cubic zinc blend phase. Int J Hydrogen Energy 2010;35:19–25.
[65] Schneider J, Bahnemann DW. Undesired role of sacrificial reagents in photocatalysis. ACS Publications; 2013.
[66] Huang C, Linkous CA, Adebiyi O, T-Raissi A. Hydrogen production via photolytic oxidation of aqueous sodium sulfite solutions. Environ Sci Technol 2010;44: 5283–8.
[67] Shangguan W, Yoshida A. Photocatalytic hydrogen evolution from water on nanocomposites incorporating cadmium sulfide into the interlayer. J Phys Chem B 2002;106:12227–30.
[68] Biswal N, Das D, Martha S, Parida K. Efficient hydrogen production by composite photocatalyst CdS–ZnS/Zirconium–titanium phosphate (ZTP) under visible light illumination. Int J Hydrogen Energy 2011;36:13452–60.